Available online at www.sciencedirect.com
ScienceDirect
Journal of the European Ceramic Society 28 (2008) 479–491
www.elsevier.com/locate/jeurceramsoc

Mullite-refractory metal (Mo, Nb) composites

J.S. Moya [a], M. Díaz [a], C.F. Gutiérrez-González [a], L.A. Diaz [b], R. Torrecillas [b], J.F. Bartolomé [a,*]

[a] *Instituto de Ciencia de Materiales de Madrid (ICMM), CSIC, Cantoblanco, 28049 Madrid, Spain*
[b] *Instituto Nacional del Carbón (INCAR), CSIC, C/Francisco Pintado Fe, 26, La Corredoira, 33011 Oviedo, Spain*

Available online 25 April 2007

Abstract

Two refractory metals were chosen as a second phase to fabricate mullite-metal composites: (a) molybdenum which is thermodynamically compatible with mullite up to 1650 °C and (b) niobium, a metal which is solid state incompatible with mullite giving rise to compounds such as NbO and Nb_5Si_3 which are both electrical conductors and more oxidation resistant than the Nb metal. The mullite-refractory metal electrically conductive composites with a content of metal (30–50 vol%) were obtained by a wet-processing route and subsequent hot pressing at 1650 °C. The effect of Mo particle size and volume fraction on the mechanical properties (σ_f, damage resistance, crack growth resistance i.e., *R*-curve behaviour, etc.) and wear resistance of the mullite–Mo composites have been assessed. Additionally these composites could be machined by electro discharge machining (EDM) technique. In the case of mullite–Nb system mullite–Al_2O_3–Nb_5Si_3–NbO composites showed electrically conducting properties. Its microstructural feature, mechanical properties (σ_f and *R*-curve behaviour) and EDM were studied and compared with the results obtained for the mullite–Mo system.

Keywords: Ceramic-metal composites; Mullite; Wear resistance; Mechanical properties

1. Introduction

New technologies request components with multiple functions or characteristics not attainable by any single phase material currently available. Composite materials formed by an insulating ceramic matrix and metallic particles, also known as cermets, have recently attracted much attention due to singular combination of properties, including mechanical, electrical and magnetic. Of the many potential ceramic-metal systems, mullite-refractory metal can be considered adequate to be used in a large number of possible applications, e.g., high/low temperature components, thermal barrier coatings,[1] electrical conductor/insulator components (HID[2] and cool LED[3] lamps), multifunctional devices, etc.

It is well known that mullite ceramics are very attractive for high temperature applications.[4,5] However, the applications of mullite as structural component are restricted because of its poor mechanical performance at room temperature.[6–9] The improvement of the mechanical properties of mullite has thus attracted much attention in the last few years.[10–13] In this regard one of the most promising approaches consists of incorporating a refractory metallic second phase as reinforcement into a mullite matrix.[14–17] The initial strategy behind their development was to use the ductile metal phase to form crack bridges following fracture of the brittle ceramic matrix. This should lead to stable crack-growth resistance behaviour (*R*-curve) and increased fracture toughness, with the consequent effect of greater strength reliability. Volume fraction of metal phase, size of ligaments, metal properties (ductility, work hardening, flow stress) and the interface properties may influence the toughening of ceramic/metal composites. Theoretical works[18,19] suggest that the fracture toughness will increase with metal volume fraction and bridge diameter.

Electrical discharge machining (EDM) is a machining process where the material is removed based on the thermal impact of successive discharges, generated between a tool electrode and a work piece, both submerged in a fluid dielectric. The EDM process allows us to machine extremely hard materials in a flexible way. Therefore, EDM is a potential and attractive technology for the machining of ceramics, provided that these materials have a sufficiently high electrical conductiv-

* Corresponding author. Tel.: +34 91 334 8996; fax: +34 91 372 0623.
E-mail address: jbartolo@icmm.csic.es (J.F. Bartolomé).

0955-2219/$ – see front matter © 2007 Published by Elsevier Ltd.
doi:10.1016/j.jeurceramsoc.2007.03.020

ity (a maximum applicable electrical resistivity of 100 Ω cm).[20] In order to meet this requirement, electro-conductive cermets can be performed by adding metal phases above the percolation threshold.

In the present study, two refractory metals were chosen as a second phase to fabricate mullite-metal composites: (a) molybdenum, because of its thermal expansion coefficient ($\alpha_{Mo} = 5.75 \times 10^{-6}\,^{\circ}C^{-1}$ at 1000 °C), very close to that of mullite ($\alpha_{Mull} = 5.13 \times 10^{-6}\,^{\circ}C^{-1}$ at 1000 °C) consequently the residual thermal stresses resulting from thermal expansion mismatch are thus expected to be negligible. The mullite–Mo system is thermodynamically stable up to 1650 °C[14]; (b) niobium, a metal which is incompatible with mullite in the solid state[21] giving rise to compounds such as NbO and Nb_5Si_3 which are both electrical conductors and more oxidation resistant than the Nb metal. As far as we know, this particular system has not been previously investigated.

2. Experimental procedure

2.1. Starting materials

The following commercially available powders have been used: (1) 99.9 mass% pure Mo metal (Goodfellow Cambridge Ltd., UK) with an average particle size of 5 μm and a specific surface area of 1.3 m^2/g; (2) 99.95 mass% pure Mo metal (H.C. Starck, Germany) with an average particle size of 10 μm and a specific surface area of 0.7 m^2/g; (3) 99.95 mass% pure Mo metal (Japan New Metal Company, Japan) with an average particle size of 25 μm and a specific surface area of 0.7 m^2/g; oxygen contents below 1 mass% in all Mo powders were detected; (4) 99.85 mass% pure Nb metal (Goodfellow Cambridge Ltd., UK) with an average particle size of 26 μm; (5) mullite (Scimarek Ltd., Japan) with an average particle size of 1.5 μm, specific surface area of 7 m^2/g, and with chemical analysis (mass%), Al_2O_3 (71.5), SiO_2 (27.3), Na_2O (0.02), MgO (0.04), CaO (0.07) and Fe_2O_3 (0.05).

2.2. Processing of mullite-(Mo,Nb) composites

The mullite-(Mo, Nb) composites were prepared following the processing route described in detail in a previous work.[15] The metal content and metal grain size of the different composites, as well as the solids loading and the amount of deflocculant used to obtain homogeneous suspensions are summarized in Table 1.

2.3. Characterization

The bulk densities of all the materials were measured using the Archimedes method, with mercury as the immersion medium.

The microstructures of fired specimens were studied on diamond polished surfaces down to 1 μm by optical microscopy (Leica, DMR model) and scanning electron microscopy (Karl-Zeiss, DSM-950 model). Interfacial phases of mullite/Nb composites were determined by using electron diffraction and energy dispersive X-ray (EDS) spectroscopy technique. The SEM-EDS configuration included a Link QX 2000 computer and a spectrometer (LINK AN-10000, Oxford) equipped with a Si–Li detector. Semiquatitative analyses were made using the ZAF correction software, based on the Cliff-Lorimer equations, with theoretical internal standards, following the RTS-2/FLS program (Link, Oxford).

The constitutional phases of the mixed powders and the composites were determined by X-ray diffraction using Cu Kα radiation.

2.4. Mechanical properties

The hot-pressed disks were machined to obtain prismatic bars with 43 mm × 3 mm × 4 mm dimensions for mechanical properties measurement. The tensile surface was polished down to 1 μm using diamond paste.

The bending strength, σ_f, was determined by three-point bending test and was conduced in loading direction perpendicular to the hot-pressing direction. Reported strengths represented the mean and standard deviation of at least 20 specimens, and were calculated according the equation:

$$\sigma_f = \frac{3QL}{2lh^2} \quad (1)$$

where Q is the failure load, L the span, l the width and h is the height. The tests were performed at room temperature using a universal testing machine (Instron Model 4411). The specimens were loaded to failure with a cross-head speed of 0.5 mm/min and a span of 40 mm.

The hardness was obtained by the Vickers indentation test. The Young's modulus was obtained from the slopes of load–deflection curves. A static extensometer was used to measure the deflection with an error in the measurement of ≈0.05%.

Table 1
Metal content and metal grain size of the different composites, as well as the vol.% of solids and the wt.% of deflocculant used to obtain homogeneous suspensions

Composite	Metal vol.%	Metal grain size (μm)	Solids loading (vol.%)	Wt% deflocculant (Dolapix PC33)
MuNb3026	30	26	43	3
MuMo305	30	5	30	1
MuMo3010	30	10	30	1
MuMo3025	30	25	30	3
MuMo5025	50	25	38	3
MuMo1025	10	25	32	3

Indentation-strength tests were performed using the prismatic bars in which the centers of the tensile faces were indented with a Vickers diamond at contact loads, P, between 10 and 500 N. The mechanical test was performed immediately after indentation to avoid any subcritical crack growth due to stress corrosion effects. The strengths, σ_f, were calculated from the failure loads, Q, and the specimen dimensions, using Eq. (1). Special effort was made to examine all specimens after testing using reflected light optical microscopy (Leica, DMR model), to verify that the indentation contact site acted as the origin of failure.

R-curves were measured via the indentation-strength method developed by Braun et al.,[22] which considers a radial crack c produced by indentation at a load P and subjected to the action of a tensile stress σ_a due to the applied stress load during three-point bending. During post-indentation bending, the crack is subjected to a total stress intensity, K_t, which is the sum of contributions from the residual stress intensity factor acting on the indentation crack resulting from the elastic-plastic mismatch associated with the indentation, K_r, and the stress intensity factor resulting from the applied stress, K_a:

$$K_t(c) = K_a(c) + K_r(c) = \psi \sigma_a c^{1/2} + \xi \left(\frac{E}{H}\right)^{1/2} \frac{P}{c^{3/2}} = K_R(c) \quad (2)$$

where ψ is the crack geometry factor, ξ the dimensionless geometrical constant, E the Young's modulus, H the hardness, and K_R is the toughness of the material. For a given indentation load, P, failure is assumed to occur at the stress where the applied stress σ_a is equal to the fracture stress, σ_f, which satisfies the following balance and tangency conditions:

$$K_t(c) = K_R(c) \quad (3)$$

$$\frac{dK_t(c)}{dc} = \frac{dK_R(c)}{dc} \quad (4)$$

The R-curve was determined by solving Eqs. (3) and (4) for each beam simultaneously. In other words, the R-curve was determined as the common envelope of the tangency points to the family of $K_t(c)$ curves from the σ_f (P) data sets.

2.5. Sliding wear test

The mullite–molybdenum composites were machined in order to obtain prismatic bars with 15 mm × 3 mm × 4 mm dimensions for sliding wear tests. The contact surfaces of the bars were polished down to surface roughness of $R_a = 0.2$ μm. Subsequently all the samples and steel discs as counterpart were washed ultrasonically in an acetone bath for 15 min, and then dried in an oven at 90 °C for 30 min. In order to assess the sliding behaviour of these materials, a pin-on-disc type wear test in air (ambient temperature of 21 °C and relative humidity of 50–70%) was carried out. A speed of 1.0 m/s and an apparent pressure of 1.0 MPa were applied on the sample pins, when sliding against 100Cr6 steel disc ($R_a = 0.5$ μm) over a period of 20 h. The sliding surface was parallel to the hot-pressing direction of the various materials. The cumulative wear rate w_C for each, pin and disc, was calculated by measuring the weight wear loss of each component Δm, after wear testing, divided by the corresponding density ρ, the applied load F_N and the sliding distance S:

$$w_C = \frac{\Delta m}{\rho F_N S} \quad (5)$$

The summation of the cumulative wear rates of the tribocouple (pin and disc) is referred to as the total cumulative wear rate. Three measurements were averaged for each material.

2.6. Nanoindentation test

Nanoindentation tests were conducted using a computer-controlled Nanotest 600 apparatus (Micro Materials limited, UK), equipped with a Berkovich type diamond indenter with 65.03° face angle. Indentations were made applying a maximun load of 150 mN, and using a loading and unloading speed of 0.73 mN/s and a holding time of 5 s after completing each indentation. The indentation load-displacement data obtained at each depth were analyzed to determine the indentation hardness (H_{IT}), or Meyer hardness, and elastic modulus, E, using the method of Oliver and Pharr.[23] In this method, the hardness and elastic modulus are evaluated from the relations:

$$H_{IT} = \frac{P_{max}}{A_{max}} \quad (6)$$

and

$$E = (1 - \nu^2)\left[\frac{1}{E_{red}} - \frac{1 - \nu_i^2}{E_i}\right]^{-1} \quad (7)$$

where P_{max} is the maximun load applied and A_{max} is the projected contact area at maximun load calculated from the contact depth (h_c) – for an ideal Berkovich indenter $A_{max} = 24.5h_c^2$ – ν the Poisson's ratio for the specimen, ν_i and E_i the Poisson's ratio and the elastic modulus of the indenter (0.07 and 1141 GPa, respectively), and E_{red} is the reduced elastic modulus obtained from the experimentally measured contact compliance, C, by the equation:

$$\frac{1}{E_{red}} = \frac{2C\sqrt{A}}{\sqrt{\pi}} \quad (8)$$

where A is the contact area. The contact compliance was determined by fitting the unloading curves to the power-law relation:

$$P = \alpha(h - h_f)^m \quad (9)$$

and numerically evaluating the derivative of the curve fit at the maximun indentation depth. In equation (9), P is the indentation load, h the indenter displacement, h_f the final indentation depth, and α and m are fitting parameters. In most stiffness evaluations, the upper 90% of the first unloading segment was used to determine the curve fitting parameters.

HV has been obtained from H_{IT} (the hardness measured directly in the nanoindentation test) through a simple conversion

using the following relation:

$$HV = 0.945 H_{IT}$$

2.7. Wire EDM machining

The thickness of the samples used in this work was 4 mm. All Wire EDM experiments have been performed on a commercial Wire-EDM machine. A brass wire electrode (*W*, 0.01 mm diameter) has been used. Observations of the topographies and cross-sections have been carried out on a scanning electron microscope.

2.8. AFM

The EDM machined surface was observed using atomic force microscopy (PSIA-XE100 AFM) in noncontact mode with a Si cantilever (Mikromash #NSC 15, force constant of 40 N/m, resonance frequency of 325 Hz). Experiments were performed in air. Prior to AFM measurements, the samples were sequentially cleaned by aqueous ammonia and de-ionized water to remove surface contaminants, and dried under nitrogen flow.

3. Results and discussion

3.1. Mullite–Mo composites

3.1.1. Microstructural analysis

The relative densities of the obtained sintered Mullite/Mo composites were found to be >99% th. Fig. 1 shows optical micrographs of the microstructures of the different mullite/molybdenum composites. Darker and bright phases are mullite and molybdenum grains, respectively. The metal particles are uniformly dispersed in the matrix and no porosity is observed, in agreement with the density measurements.

3.1.2. Mechanical properties

The Young's modulus, hardness and bending strength for the studied specimens are given in Table 2.

The Young's modulus of the composites was found to be very close to values predicted by the rule of mixtures. The hardness of all the composites decreases because of the lower hardness of Mo polycrystals (2.1 GPa) compared to mullite.[24]

The fracture strength of the un-indented mullite/molybdenum composites varied depending on the molybdenum volume frac-

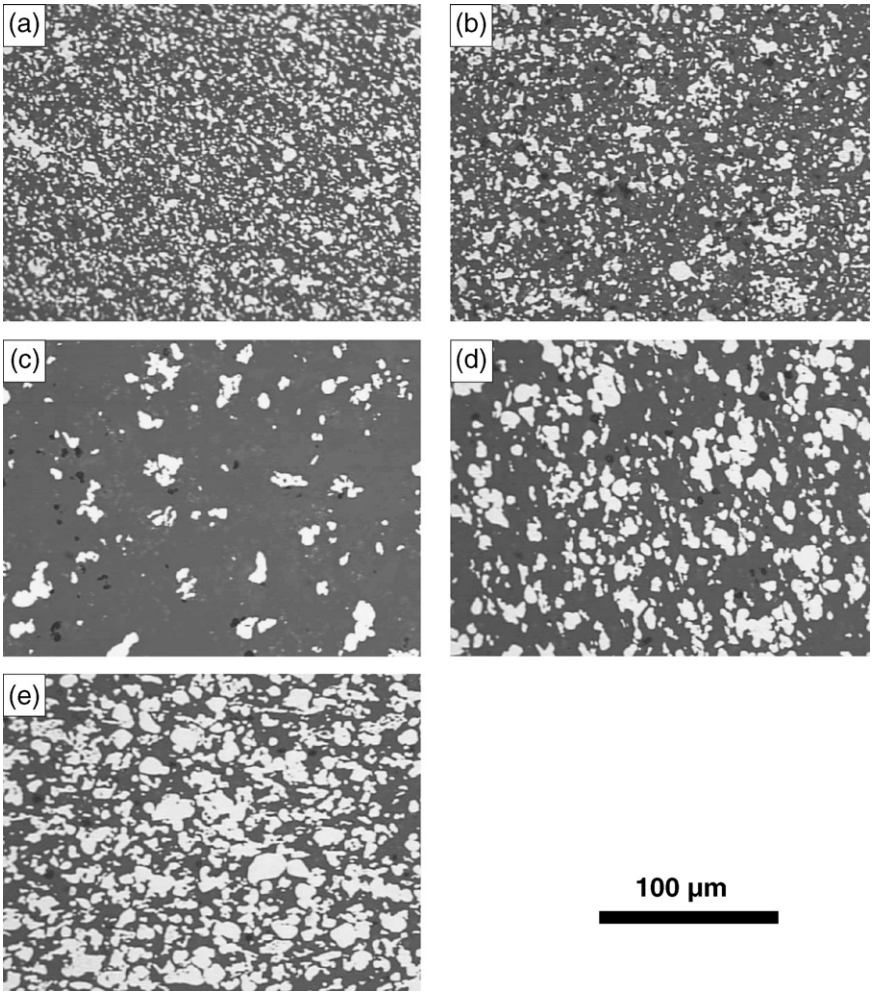

Fig. 1. Optical micrographs of different mullite–Mo composites: (a) MuMo305, (b) MuMo3010, (c) MuMo1025, (d) MuMo3025 and (e) MuMo5025.

Table 2
Three-point bending strength, Young's modulus, mean Vickers hardness and damage tolerance index of mullite-refractory metal composites

Material	σ_f (MPa)	HV (GPa)	E (GPa)	D_t ($m^{1/2}$)
MuMo305	530 ± 15	7.3	242	0.438
MuMo3010	435 ± 25	7.3	242	0.762
MuMo1025	291 ± 10	10.9	205	0.323
MuMo3025	227 ± 9	7	175	1.101
MuMo5025	380 ± 13	5.3	247	2.207
MuNb3026	240 ± 20	12	290	0.805
Mullite	320 ± 15	11	220	0.125

tion and grain size. The σ_f values for MuMo305 and MuMo3010 were found to be about 65% and 35% higher than the monolithic mullite. In the case of MuMo3025 the σ_f value was about 15% lower than the mullite. That is, the smaller the Mo grain size the smaller is the critical flaw of the composites, and consequently the σ_f value is increased. In the case of MuMo5025 the strength value was found to be higher than the other two composites with similar Mo grain size (MuMo1025 and MuMo3025) due to the highest fracture toughness value.

The fracture strength as a function of indentation load for monolithic mullite and mullite/molybdenum composites is shown in Fig. 2. From such graphs the asymptotic slope can be used as an indicator of the damage tolerance of the material. Each datum point represents the mean and standard deviation of on average, 20 indentation-flaw failures. Also plotted, for comparison purpose, is the best fit of a constant toughness material strength response corresponding $P^{-1/3}$ asymptote. The strengths for natural flaws of different materials were arbitrarily plotted at $P = 1$ N. Great care was taken to ensure that the indentation site was the source of the critical flaw for all reported data. Linear regression was used to obtain the best fit for the data from monolithic mullite and mullite–molybdenum composites. It showed that the slopes of monolithic mullite, MuMo305, MuMo3010, MuMo1025, MuMo3025 and MuMo5025 composites were 0.32, 0.22, 0.17, 0.18, 0.05 and 0.05, respectively. For perfectly brittle materials the slope corresponds to 1/3. The asymptotic slope for the mullite–Mo composites in Fig. 2 is less than 1/3. The improved strengths displayed by the composites at higher loads (large flaws) are evidence which suggest that they are damage tolerance materials. Recently, Bao et al.[25] has proposed a method to quantitatively estimate the damage tolerance of ceramics (D_t). According to this method, damage tolerance depends on the flaw tolerance and the energy dissipation capacity of the material, and it can be defined by the following equation:

$$D_t = \frac{K_{IC}}{\sigma_f}\frac{E}{H} \tag{10}$$

where K_{IC}, σ_f, E and H are toughness, bending strength, Young's modulus and hardness, respectively. K_{IC}/σ_f is associated with the resistance to crack extension, while E/H comes from the capacity of local energy dissipation. The damage tolerance index D_t of the different materials are listed in Table 2. The MuMo3025 and MuMo5025 composites, with the larger Mo average grain size and higher volume fraction of metal, have higher indentation strength and damage tolerance index than the other composites and monolithic mullite. On the other hand, the monolithic mullite is a single-value toughness ceramic, and shows a classical flaw sensitivity in the strength characteristics, as shown by a $P^{-1/3}$ load dependency. The value of the damage tolerance index, in this particular case, is very low and comparable with other brittle materials.[25] D_t as a function of Mo grain size for Mo–mullite composites reinforced with 30 vol% of metal and monolithic mullite are shown in Fig. 3a. As can be observed, the D_t increase with the Mo grain size, and show a maximum at 25 μm Mo grain size (MuMo3025). Taking into account the strength of the same materials, data for surfaces in their as-polished state (filled symbols) and after predamage from Vickers indenter at a prescribed load $P = 50$ N (unfilled symbols) are plotted in Fig. 3b. In the case of as-polished specimens, σ_f increases monoton-

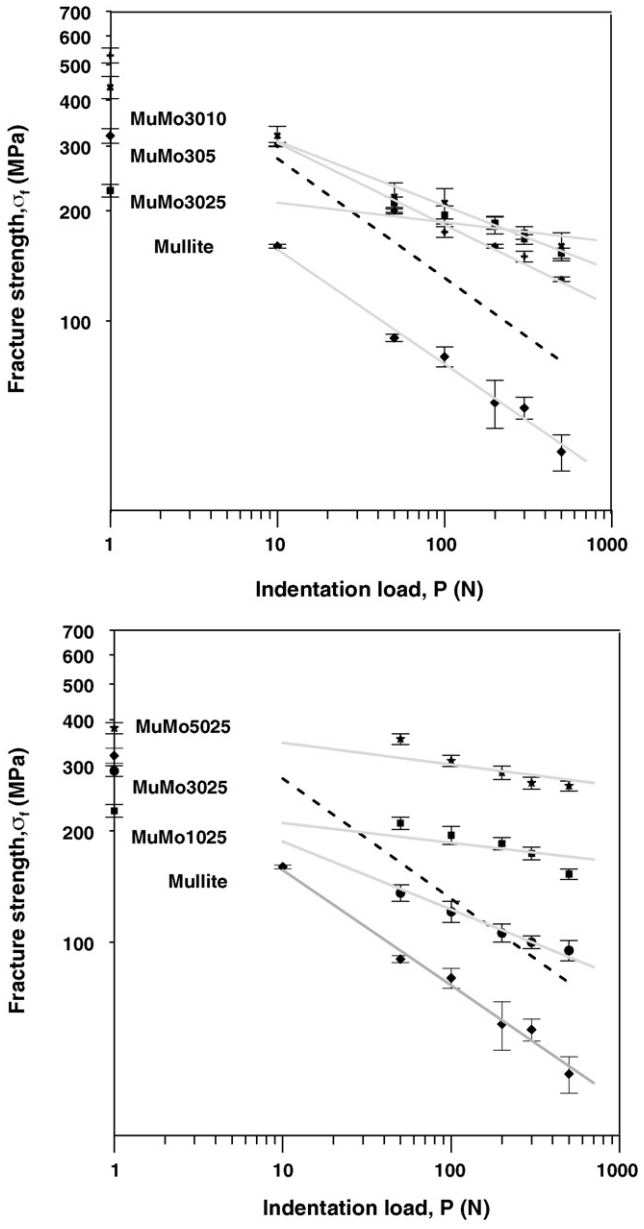

Fig. 2. Indentation load vs. strength plots of monolithic mullite and mullite–molybdenum composites. The indentation-strength data to the $P^{-1/3}$ strength response is shown by the diagonal dashed line.

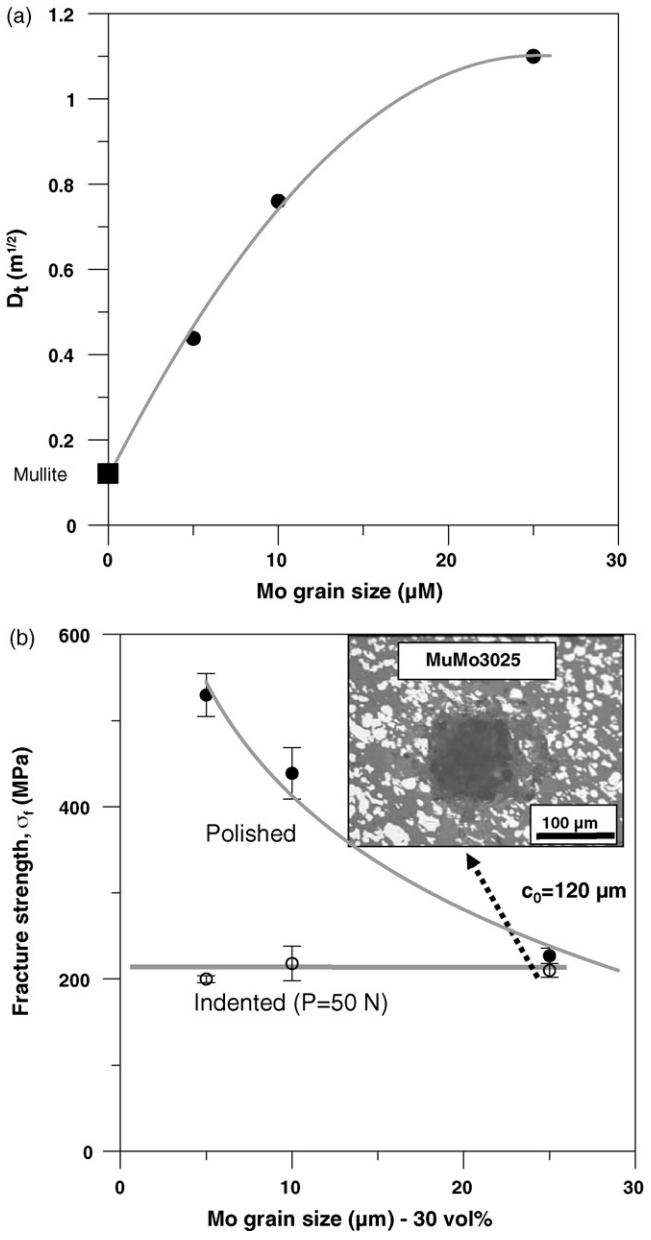

Fig. 3. (a) Damage index (D_t) vs. Mo grain size plot of mullite–molybdenum composites; (b) strength of composites as a function of Mo grain size (c_0 is the initial flaw size). An optical micrograph of Vickers indentation in MuMo3025 material is inserted.

ically with decresing Mo grain size, as expected. In the case of MuMo3025 composites, the value of as-polished and preindented strength (the Vickers indentation dimension is ≈120 μm, five times higher than the intrinsic flaw) is similar. Therefore, this composite offers an optimal compromise between strength and damage tolerance.

The σ_f versus P measurements were subsequently used to deconvolute the R-curve, in accordance with an indentation-strength K-field analysis of Braun et al.[22] described above. For the present study, the value of ψ was taken to be 1.29, as used in previous work,[26] assuming that the crack geometry produced by Vickers indentation is material-independent. The value of the geometrical constant $\xi = 0.016$ calibrated by Anstis et al.[27] from a number of brittle materials with known values that has been widely used in the literature,[12,28,29] and appropriate E and H values from Table 1, were used to generate these plots. The resulting R-curves have been plotted in Fig. 4. These experimental results obtained with indentation strength test show that the mullite–molybdenum composites develop "crack growth resistance". In contrast, monolithic mullite shows no such rising R-curve, consistent with its transgranular fracture mode and consequent lack of wake bridging. In this particular case, the toughness is found to be nearly equal to the measured toughness ($K_{IC} = 2\,MPa\,m^{1/2}$). The crack growth resistance, and therefore the flaw tolerance, is more important in MuMo5025 composite because the volume and grain size of the molybdenum second phase is larger and the number of molybdenum grains involved in crack bridging is higher than in the other composites. The

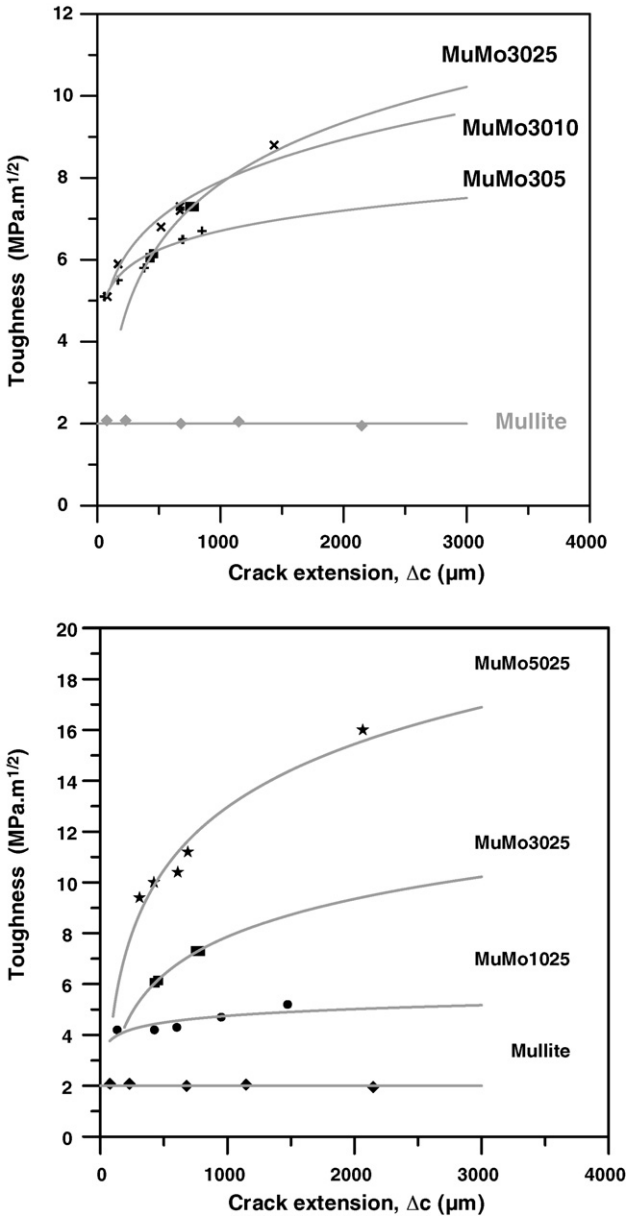

Fig. 4. Predicted fracture resistance curves (R-curves) as a function of crack size for mullite and mullite–Mo composites.

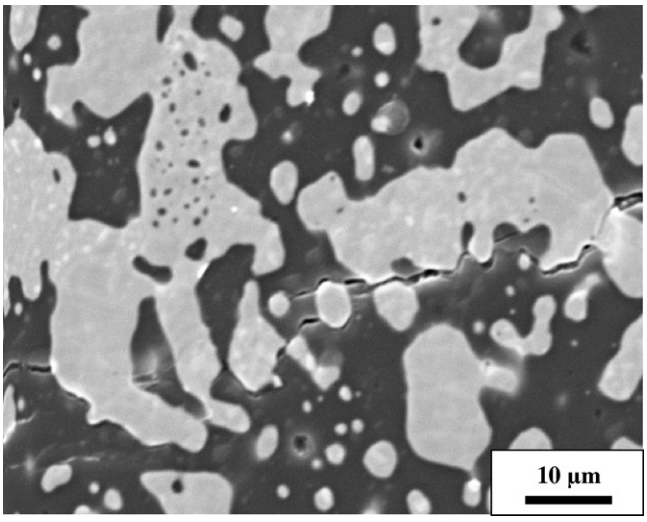

Fig. 5. Stretched Mo ligaments bridging the crack faces in MuMo3010 composite.

increment in toughness value observed in these composites can be assigned to a crack bridging by the plastic deformation of the metallic particles as can be deduced from the SEM micrographs shown in Fig. 5. Once the crack has reached the particle-matrix interface, the difference in the crack-tip opening displacement between the ductile particle and the brittle matrix will cause the crack to be locally blunted and its segments forced to circumvent the particle, and consequently bridging the crack along its length. Thus, on applying an external load to the sample, these ligaments impose closure traction on the crack surface against the opening of the crack that transfer more of the far field stress to the developing bridged-zone, requiring higher applied stress intensities to propagate the crack tip. This toughening mechanism requires both (i) strong metal-ceramic bonding and (ii) a high plasticity of the metal particles. Interfaces that are strengthened mechanically are believed to increase the toughness of the composite by reducing the possibility of premature metal-particle pull-out during crack propagation in the ductile-phase-toughened brittle materials.

It is important to point out that the plasticity of Mo is strongly dependent on the oxygen content.[30] In order to study the effect of oxygen content on the plasticity of molybdenum, monolithic mullite and mullite doped with 8 wt% of MoO_2 ceramics were joined by hot pressing at 1650 °C (solid state diffusion bonding), using a Mo metal interlayer.[31] Fig. 6a shows Vickers indentation near the mullite–Mo interfaces on polished cross-sections using a 50 kg load in ambient air. As can be observed, the Mo foil exhibits plastic deformation and the crack generated under indentation test does not propagate into the metal. Conversely, in the mullite–MoO_2/molybdenum/mullite–MoO_2 sample the presence of a multiple cracks inside the metal can be observed (Fig. 6b), suggesting an embrittlement effect. Therefore, to improve the toughness of mullite/Mo composites, it is important to control the amount of oxygen in Mo and the content of Mo oxides in the starting powder.[14] Reduction with hydrogen eliminates the oxygen which can segregates to grain boundaries and precipitates as Mo oxides, increasing the intergranular fracture stress and promoting plastic deformation.

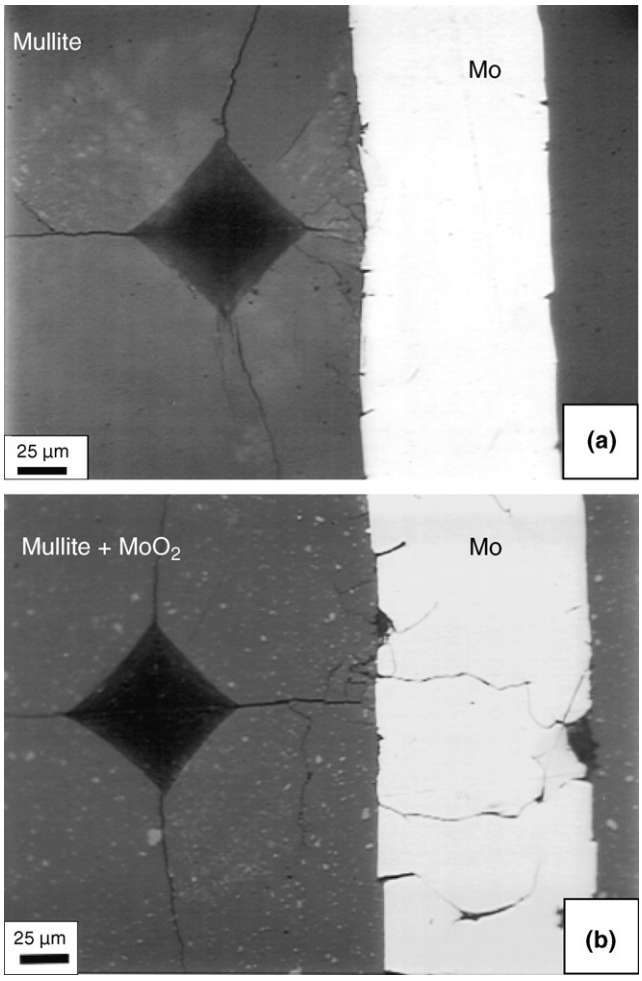

Fig. 6. Vickers indentation near the interfaces on polished cross-sections of: (a) mullite–Mo interlayer and (b) mullite/MoO_2–Mo interlayer.

3.1.3. Sliding wear against steel

In Fig. 7 the cumulative wear rate of the tribocouple (as the sum of the specific wear rates of the pin and disk counterpart) of the mullite/Mo composites with different Mo grain sizes and contents, as well as those corresponding to the monolithic mullite and pure Mo (for comparative purposes) are shown. As it can be observed, the optimum combination for the size and the amount of metal phase corresponds to the composite MuMo3025, which contains a metal volume fraction of 30% with Mo grain size of ≈25 μm. The composites that possess metal phase more than 30 vol% showed extruded tribofilms created on the surface. On the other hand, there were no obvious tribofilms but many grooves due to abrasive wear on the composites with 10 vol% of Mo. Metal phases were fractured and removed out from the system. This implies that a certain amount of metal phase in ceramic matrix is required in order to create protective tribofilms.

The wear mechanism of the ceramic/metal composites is a combination of abrasive wear by hard ceramic asperities and par-

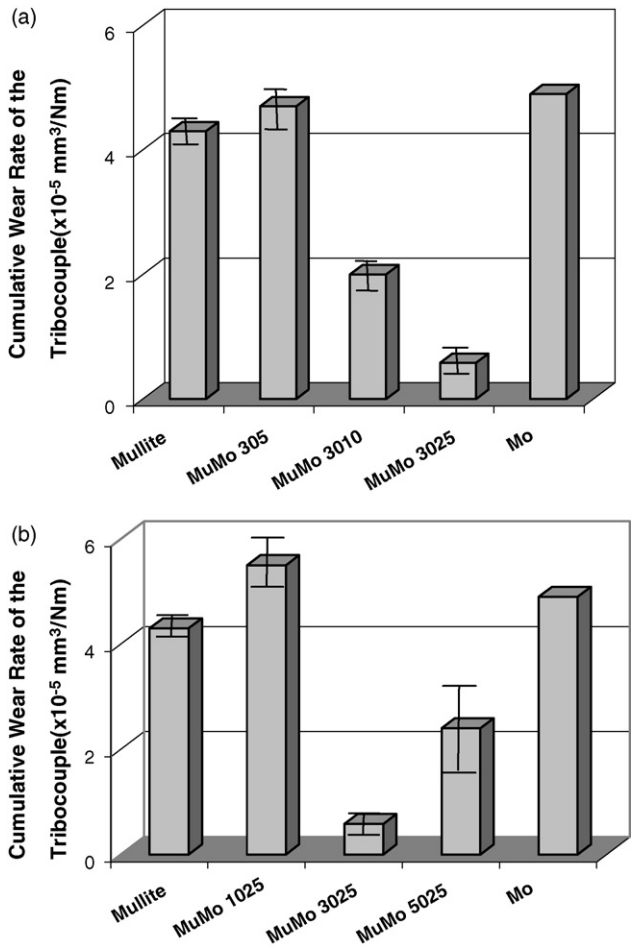

Fig. 7. Cumulative wear rate of the tribocouple of the different mullite/Mo composites as a function of metal grain size (a), and Mo volume fraction (b). The monolithic mullite and pure Mo have been included for comparative purposes.

ticles and adhesive wear between the metallic components. From the experimental evidences, it is deduced that the abrasive wear mechanism is dominant when the composite has small amount of metal phase, and the contribution of the abrasive wear decreases with an increase of the amount of Mo up to the optimum value of 30 vol%. However, abrasive wear mechanism contributes with increasing the amount of metal, and it becomes dominant when the composite has a significant amount of Mo, e.g., more than 50 vol% (see Fig. 7). On the other hand, for the same Mo content the abrasive mechanism becomes dominant with the decrease of the metal particle size. This wear mechanism is suppressed in the case of composites with large metal particles, because the isolated areas of both ceramic and metal phases on the sliding surface are larger than in the composites with small metal particles. Moreover, the area of the adhered and extruded metal on the sliding surface, which can deform plastically and absorb impact energy, i.e., it plays a cushioning role against hard particle abrasion, is larger than in the composite with smaller metal particle size. At the same time, the presence of ceramic prevents the occurrence of adhesive wear of metals. Furthermore, the larger the Mo grain size, larger *R*-curve behaviour of the mullite/Mo composites, due to the increase of bridging mechanism by plastic deformation of metal particles, which prevent the crack growth and, thus, the ceramic-metal debonding, improving the wear resistance.

Taking into account these tendencies, the experimental data can be fitted to logistic sigmoidal equations[32] that allow to describe the behaviour against the sliding wear of the mullite/Mo composites in terms of the accumulation of both abrasive and adhesive components, which results in a (positive) synergistic effect depending on the grain size and the amount of metal in the ceramic matrix. It can be concluded that at least 30 vol% of Mo is required regardless of the metal grain size, in order to obtain the synergistic effect from the combination and minimize the cumulative wear rate by the self-lubricanting tribofilm creation.

When the cumulative wear resistance of the tribocouples is compared with the hardness of the composites, the monolithic ceramic and the pure metal, there is no significant change for the materials tested against steel, except for the ceramic/metal composite with the optimized amount and size of metal phase, MuMo3025. Such ceramic/metal composite could achieve high wear resistance even with relativity low hardness due to the above mentioned synergistic effect. MuMo3025 versus 100Cr6 tribo-pair showed one order of magnitude lower cumulative wear rate than the monolithic mullite or pure molybdenum against steel, and four times better than 100Cr6 versus 100Cr6 tribo-pair, which is used as a standard bearing material.[32]

3.1.4. Wire EDM machining

The electrical resistivity (measured by four-wire ohmmeter) of the mullite–Mo composites with a metal content above the percolation threshold[33] (∼16 vol.%) was found to be $<2 \times 10^{-4}\ \Omega$ cm. in all samples. This value is about 6 orders of magnitude less than the limit of 100 Ω cm, which make the material suitable for EDM. In consequence all the samples (except MuMo1025) were able to be EDM. A typical SEM micrograph of the cross-section of the machined samples is shown in Fig. 8. As can be observed the cross-section

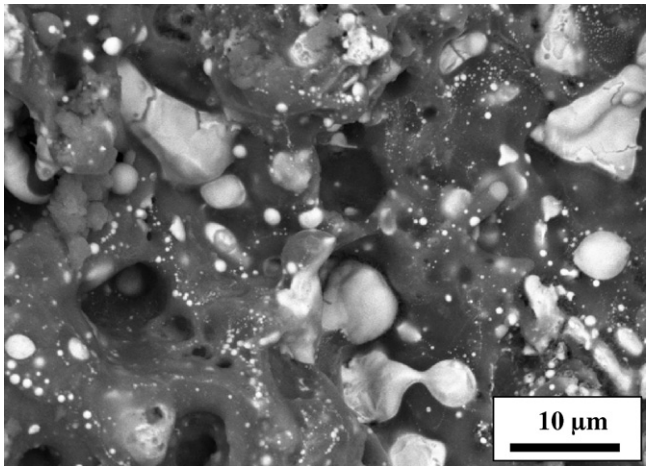

Fig. 8. SEM micrograph of the surface roughness of mullite–Mo composite machined under EDM condition.

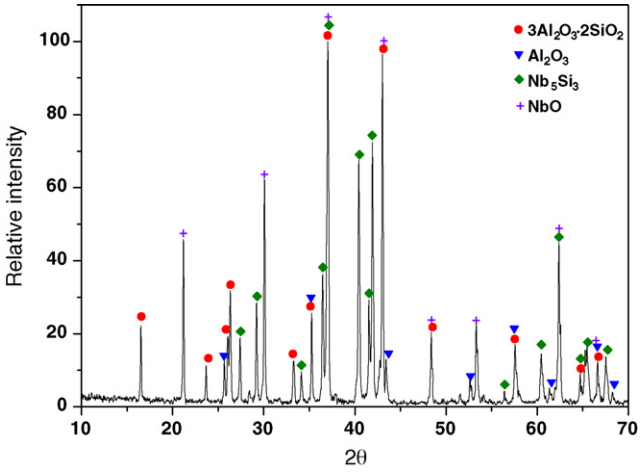

Fig. 9. XRD pattern of mullite–Nb composite.

of the rough machined sample shows many droplets and microcracks. This indicates that the material removal mechanism is most probably melting/evaporation. The wireEDMed surface (e.g., droplets and voids) and subsurface quality (e.g., formation of microcracks) are quite complex and depend not only on the generator settings but also on the material properties like melting point, thermal conductivity and toughness.

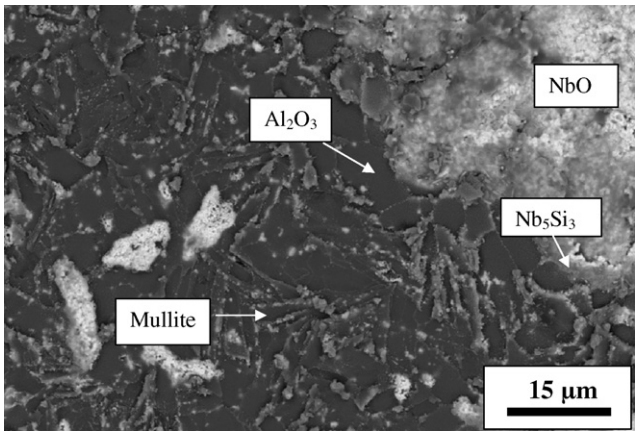

Fig. 11. Grain structures of a thermally etched surfaces of mullite–Al_2O_3–Nb_5Si_3–NbO "in situ" composites.

3.2. Mullite–Nb composites

3.2.1. Microstructural analysis and high temperature incompatibilities

The XRD pattern of the compact obtained after sintering at 1650 °C of mullite–Nb powder is shown in Fig. 9. The absence of reflections corresponding to Nb metal together with the presence of diffraction peaks belonging to Nb_5Si_3, NbO and Al_2O_3 indicates that the mullite–Nb system is incompatible at that tem-

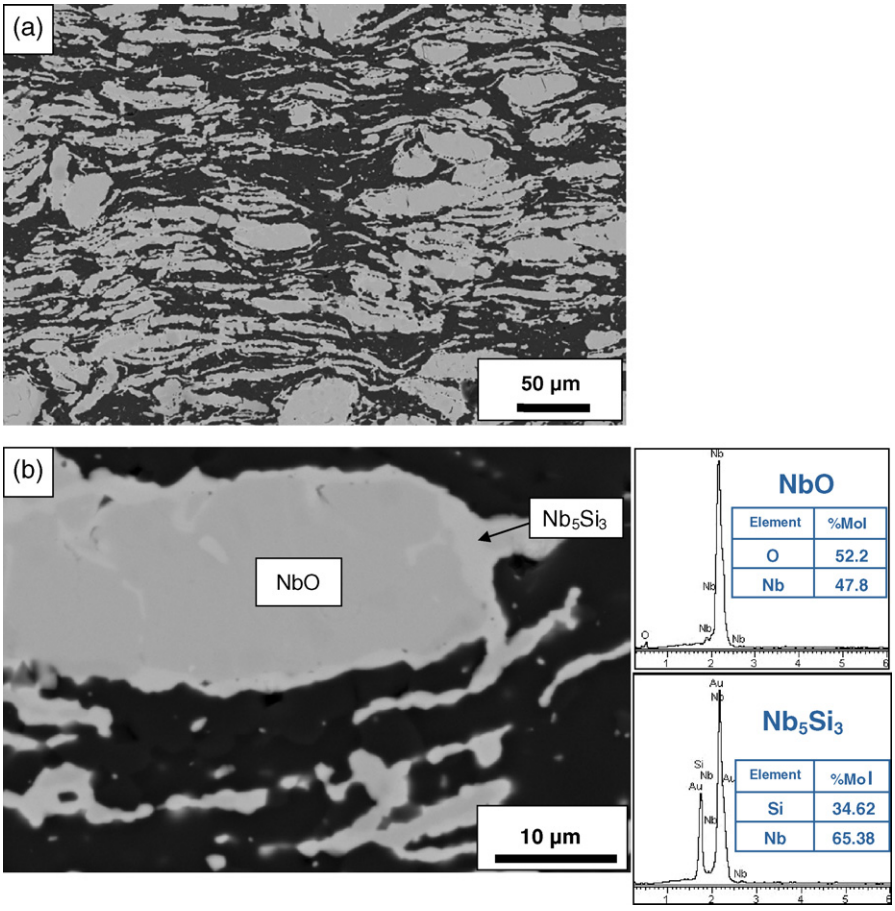

Fig. 10. (a) Microstructure of this in situ formed mullite–Al_2O_3–Nb_5Si_3–NbO composite; (b) close up of a NbO grain and EDS spectra of different regions.

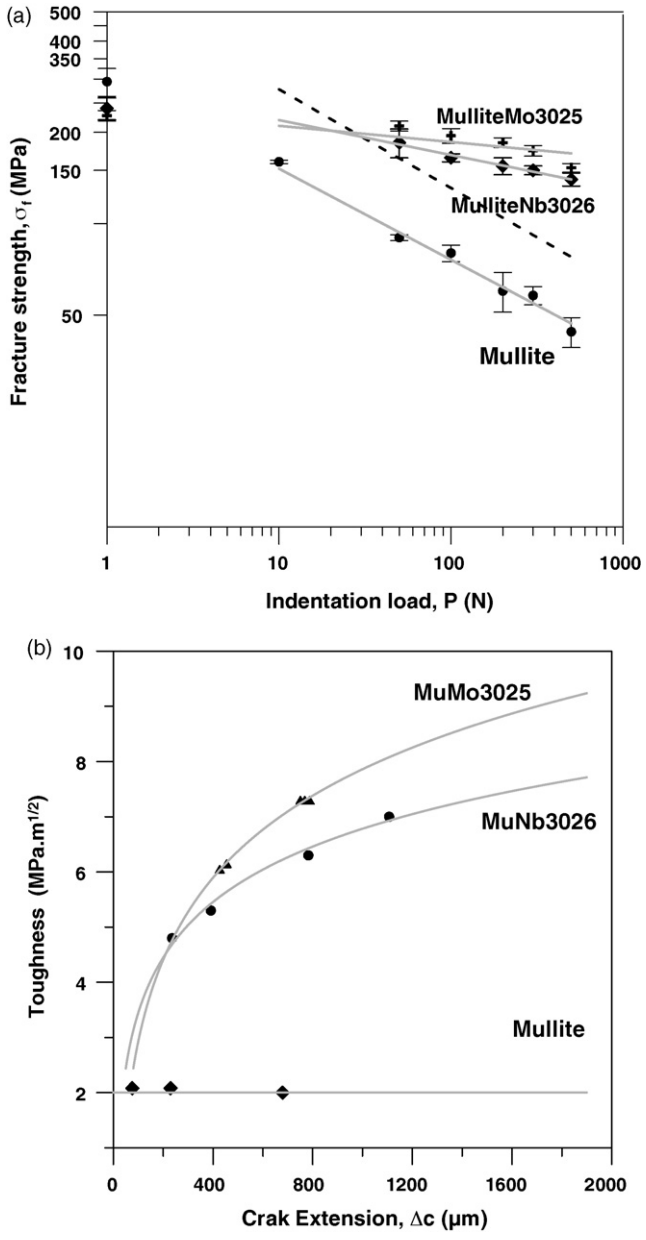

Fig. 12. (a) Indentation load vs. strength plots and (b) predicted fracture resistance curves (*R*-curves) as a function of crack size of monolithic mullite and mullite–Al_2O_3–Nb_5Si_3–NbO "in situ" composites. Results of MulliteMo3025 composite are plotted for comparative purposes.

perature in a low oxygen partial pressure (hot-press sintering conditions). In fact, this is in agreement with the phase diagram of Nb–Si–O ternary system reported by Fujiwara et al.[21] According to the isothermal section at 1650 °C (1923 K), there is a three-phase compatible triangle that involves the thermodynamically stable species Nb_5Si_3, NbO and SiO_2. Taking into account that metallic niobium and SiO_2 can never co-occur in Nb–Si–O ternary system and the XRD results, the following reaction between mullite and metallic Nb, involving the decomposition of mullite, is proposed[34]:

$$3/2Al_6Si_2O_{13} + 11Nb \rightarrow Nb_5Si_3 + 6NbO + 9/2Al_2O_3,$$
$$\Delta G(1923) = -265\,\text{kJ mol}^{-1} \quad (1)$$

Table 3
Mean hardness and reduced elastic modulus values for the different compounds of mullite–Al_2O_3–Nb_5Si_3–NbO composite determined by nanoindentation

Material	HV (GPa)	E_{red} (GPa)
Mullite	13	240
Al_2O_3	20	318
Nb_5Si_3	16	310
NbO	14	302

The microstructure of this in situ formed mullite–Al_2O_3–Nb_5Si_3–NbO composite is shown in Fig. 10. Semi-quantitative energy dispersive X-ray (EDS) spectroscopy revealed chemical compositions of the constituent phases. Fig. 11 shows the grain structure of thermally etched surface of composites. The intermetallic phase Nb_5Si_3 is mainly formed at the grain boundary of the Nb particles, with the decomposition of the mullite and the formation of typical pseudohexagonal alumina grains. The interfacial reaction between Nb and mullite should be controlled by the SiO_2 diffusion from the mullite region to the Nb region. Nb is capable of reducing SiO_2 to form Nb_5Si_3, releasing oxygen that diffuses inside the Nb particle and forms NbO. This formation mechanism of metal-silicides interlayers has also been observed for other systems, i.e., the reaction between high SiO_2 content bioglasses and Ti to form a Ti_5Si_3 interlayer.[35,36]

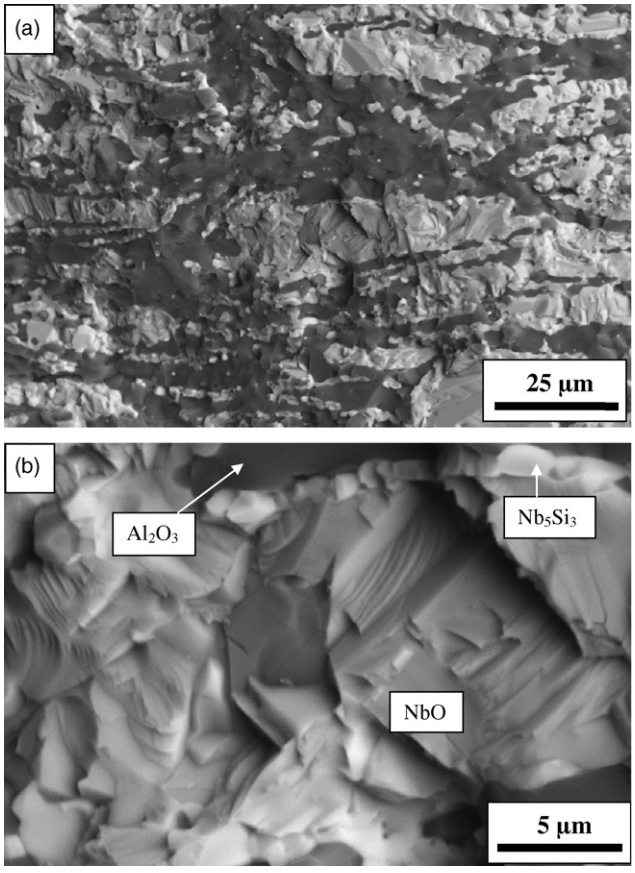

Fig. 13. (a) Fracture surface in a mullite–Al_2O_3–Nb_5Si_3–NbO "in situ" composite; (b) close up of fracture mode of Al_2O_3, Nb_5Si_3 and NbO.

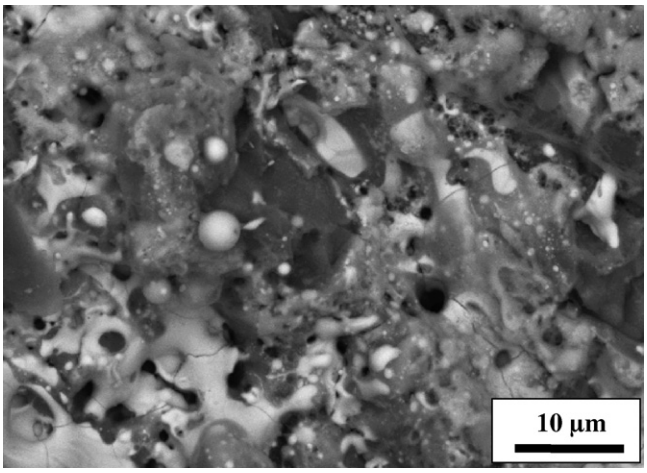

Fig. 14. Morphology of the EDM surface of mullite–Al_2O_3–Nb_5Si_3–NbO composite showing melt-formation droplets and microcracks.

3.2.2. Mechanical properties

The bending strength, Young's modulus and hardness of the mullite–Al_2O_3–Nb_5Si_3–NbO composite are given in Table 2. The reduced elastic modulus and Vickers hardness of the different constituent phases of the composite were determined by nanoindentation (Table 3).

The fracture strengths as a function of indentation load for monolithic mullite and mullite–Al_2O_3–Nb_5Si_3–NbO composite are shown in Fig. 12a. Each datum point represents the average and standard deviation of 20 indentation-flaw failures. For comparison the data of the mullite–Mo composite with similar metal grain size are plotted. It showed that the slopes of monolithic mullite, MuMo3025 and MuNb3026 composites were 0.32, 0.05 and 0.12, respectively. Fig. 12b compares the *R*-curves of the composites with the monolithic mullite. These experimental results obtained with indentation strength test show that the mullite–Al_2O_3–Nb_5Si_3–NbO composites develop "crack growth resistance", associated with the development of a steady-state bridging zone.

Typical SEM photomicrographs of the fracture surface are presented in Fig. 13. Fracture of the composite occurred predominantly via cleavage through the larger NbO grains. This micrograph also shows a clear evidence of plasticity, i.e., intersecting slip bands, within the deforming niobium oxide particles. This mechanism is favoured by the strong adherence of the NbO grains to the matrix (mullite + Al_2O_3) because of the intermetallic (Nb_5Si_3) interlayer (Fig. 10b).

3.2.3. Wire EDM machining

Nb_5Si_3 and NbO are the electrically conducting phases of the mullite–Al_2O_3–Nb_5Si_3–NbO composite. The electrical resistivity (measured by four-wire ohmmeter) of this composite was found to be $\approx 2 \times 10^{-3}\ \Omega$ cm which is about one order of magnitude higher than the one corresponding to the mullite–Mo composites, but far away from the threshold value of 100 Ω cm which makes the material suitable for EDM. The NbO phase is a hard ceramic material characterized by an electrical resistivity at room temperature of $\approx 2 \times 10^{-5}\ \Omega$ cm.[37] On the other hand, Nb_5Si_3 has an electrical resistivity at room temperature

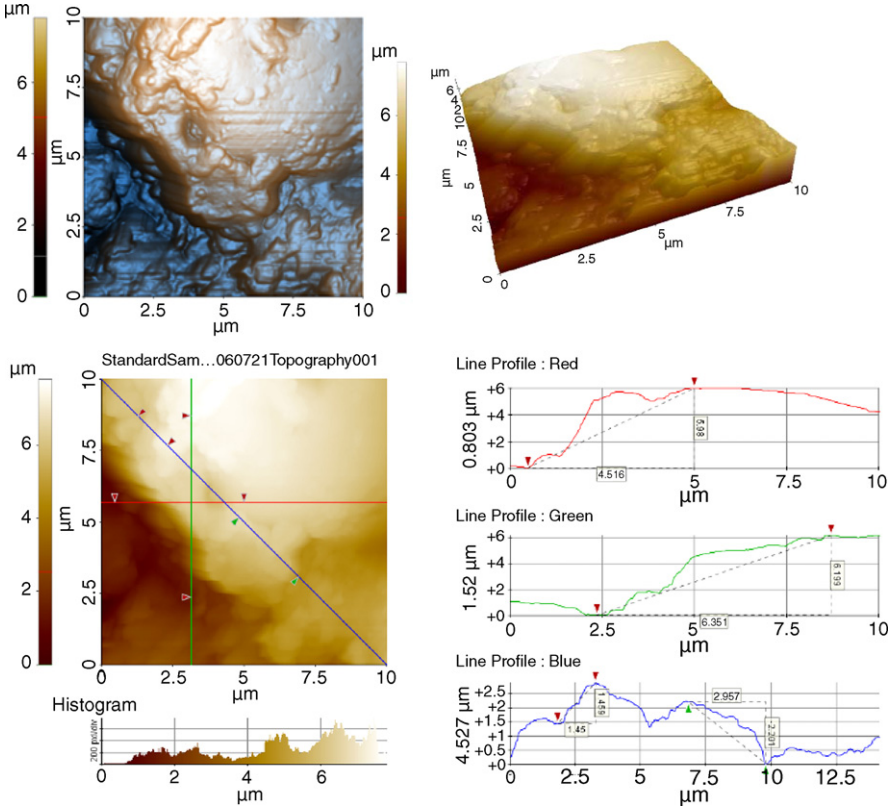

Fig. 15. AFM image of 25 μm × 25 μm scans for EDM machined mullite–Al_2O_3–Nb_5Si_3–NbO sample.

of $\approx 1 \times 10^{-3}\ \Omega\,cm$.[38] A typical SEM micrograph of the cross-sections of the rough machined samples showing many droplets and microcracks is shown in Fig. 14. This cross-section was studied by AFM. In Fig. 15 the roughness as well as the typical surface morphology are shown. The surface roughness (arithmetic deviation from the mean line through the complete profile) was found to be $R_a = 1.6 \pm 0.5\ \mu m$.

4. Conclusions

We have obtained mullite based electrical conductor composites with different microstructures. The following results can be drawn:

1. The composites of mullite matrix reinforced with a ductile isolated Mo phase exhibited progressively weaker sensitivity of strength to indentation load (flaw size) with increasing volume and grain size of Mo. The increase in the resistance of these ceramic matrix composites with adherent ductile phase to crack propagation with crack extension (rising *R*-curve behaviour) can be attributed to clamping forces applied by metal ligaments that bridge the crack faces behind the crack front. Mullite/Mo composites could achieve high wear resistance even with a relativity low hardness due to the synergistic effect of volume fraction plus grain size of the metal (30 vol% and 25 μm) decreasing both the adhesive and the abrasive wear mechanisms by the self-lubricating tribofilm creation.
2. In situ formation of mullite–Al_2O_3–Nb_5Si_3–NbO composites show an interpenetrating microstructure with strong matrix-particle interfacial reactions. These composites may be considered as potential structural material for high temperature applications in the aerospace industry because they possess high melting point, low density, high damage tolerance and *R*-curve behaviour at room temperature and excellent oxidation resistance up to 1500 °C. Furthermore, its EDM characteristics suggest that these composites can be machined to complex shapes.

Acknowledgements

This work was supported by EU under project reference FP6-515784-2, by the Spanish Ministry of Science and Technology under projects numbers MAT2003-04199-C02 and MAT2006-10249-C02-01. J.F.B. has been supported by Ministry of Science and Technology and CSIC under the "Ramón y Cajal" Program co-financed by European Social Fund. M. Díaz has been supported by Spanish Ministry of Education and Science and CSIC under I3P Program financed by European Social Fund. The authors thank Dr. K. Kameo for help in wear test.

References

1. Jin, G., Takeuchi, M., Honda, S., Nishikawa, T. and Awaji, H., Thermal shock testing on mullite/Mo FGM diks using an infrared radiation/water flow technique. *J. Ceram. Soc. Jap.*, 2004, **112**(5), S286–S290.
2. Umemoto, A., Hayashi, K., Kakashima, K., Saito, N., Kaneko, K. and Ogi, K., High-intensity discharge lamp with Mo-SiO_2 functionally graded material. *J. Am. Ceram. Soc.*, 2006, **89**(3), 1133–1135.
3. Janeway, P. A., Lighting in the solid state. *Am. Ceram. Soc. Bull.*, 2006, **85**(5), 17–20.
4. Aksay, I. A., Dabbs, D. M. and Sarikaya, M., Mullite for structural, electronic, and optical applications. *J. Am. Ceram. Soc.*, 1991, **74**(10), 2343–2358.
5. Torrecillas, R., Fantozzi, G., De Aza, S. and Moya, J. S., Thermomechanical behaviour of mullite. *Acta Mater.*, 1997, **45**(3), 897–906.
6. Mahn, T.-I. and Mazdiyasni, K. S., Mechanical properties of mullite. *J. Am. Ceram. Soc.*, 1983, **66**(10), 699–703.
7. Kanzaki, S., Tabata, H., Kumazawa, T. and Ohta, S., Sintering and mechanical properties of stoichiometric mullite. *J. Am. Ceram. Soc.*, 1985, **68**(1), C-6–C-7.
8. Ismail, M. G. M. U., Nakai, Z. and Somiya, S., Microstructure and mechanical properties of mullite prepared by the sol–gel method. *J. Am. Ceram.Soc.*, 1987, **70**(1), C-6–C-7.
9. Ohnishi, H., Kawanami, T., Nakahira, A. and Niihara, K., Microstructure and mechanical properties of mullite ceramics. *Yogyo Kyokaishi*, 1990, **98**(6), 541–547.
10. Rezaie, H. R., Rainforth, W. M. and Lee, W. E., Fabrication and mechanical properties of SiC platelet reinforced mullite matrix composites. *J. Eur. Ceram. Soc.*, 1999, **19**, 1777–1787.
11. Gao, L., Jin, X., Kawaoka, H., Sekino, T. and Niihara, K., Microstructure and mechanical properties of SiC–mullite nanocomposite prepared by spark plasma sintering. *Mater. Sci. Eng.*, 2002, **A334**, 262–266.
12. Bartolomé, J. F., Moya, J. S., Requena, J., Llorca, J. and Anglada, M., Fatigue crack growth behavior in mullite/alumina functionally graded ceramics. *J. Am. Ceram. Soc.*, 1998, **81**(6), 1502–1508.
13. Moya, J. S. and Osendi, M. I., Microstructure and mechanical properties of mullite/ZrO2 composites. *J. Mater. Sci.*, 1984, **19**(9), 2909–2914.
14. Bartolomé, J. F., Díaz, M., Requena, J., Moya, J. S. and Tomsia, A. P., Mullite/molybdenum ceramic-metal composites. *Acta Mater.*, 1999, **47**(14), 3891–3899.
15. Bartolomé, J. F., Díaz, M., Requena, J. and Moya, J. S., Influence of the metal particle size on the crack growth resistance in mullite/molybdenum composites. *J. Am. Ceram. Soc.*, 2002, **85**(11), 2778–2784.
16. Jayaseelan, D. D., Rani, D. M., Nishikawa, T., Awaji, H. and Ohji, T., Sintering and microstructure of mullite-Mo composites. *J. Eur. Ceram. Soc.*, 2002, **22**, 1113–1117.
17. Sivakumar, R., Jayaseelan, D. D., Nishikawa, T., Honda, S. and Awaji, H., Influence of MgO on microstructure and properties of mullite-Mo composites fabricated by pulse electric current sintering. *Ceram. Inter.*, 2001, **27**(5), 537–541.
18. Sigl, L. S., Mataga, P. A., Dalgleish, B. J., McMeeking, R. M. and Evans, A. G., On the toughness of brittle materials reinforced with a ductile phase. *Acta Metall.*, 1988, **36**, 945.
19. Rühle, M. and Evans, A. G., High toughness ceramics and ceramic composites. *Prog. Mater. Sci.*, 1989, **33**, 85.
20. Koning, W., Dauw, D. F., Levy, G. and Panten, U., EDM—future steps towards the machining of ceramics. *Ann. CIRP*, 1988, **37**(1), 623–631.
21. Fujiwara, H., Ueda, Y., Awasthi, A., Hrishnamurthy, N. and Garg, S. P., Determination of standard free energy of formation for niobium silicides by emf measurements. *J. Electrochem. Soc.*, 2003, **150**(8), J43–J48.
22. Braun, L. M., Benninson, S. J. and Lawn, B. R., Objective evaluation of short-crack toughness curve using indentation flaws: case study on alumina-based ceramics. *J. Am. Ceram. Soc.*, 1992, **75**(11), 3049–3057.
23. Oliver, W. C. and Pharr, G. M., An improved technique for determining hardness and elastic-modulus using load and displacement sensing indentation experiments. *J. Mater. Res.*, 1992, **7**, 1564.
24. Smithells, C. S., *Metals references book, 3*. Butterworths, London, 1967, pp. 917.
25. Bao, Y. W., Hu, C. F. and Zhou, Y. C., Damage tolerance of nanolayer grained ceramics and qualtitative estimation. *Mater. Sci. Technol.*, 2006, **22**(2), 227–230.

26. Torres, Y., Anglada, M., Llanes, L., Bartolomé, J. F., Díaz, M. and Moya, J. S., Fracture and fatigue behaviour of mullite/molybdenum composites. *Key Eng. Mater.*, 2005, **290**, 110–120.
27. Anstis, G. R., Chankitul, P., Lawn, B. R. and Marshall, D. B., A critical evaluation of indentation techniques for measuring fracture toughness: I. *J. Am. Ceram. Soc.*, 1981, **64**(9), 533–538.
28. Cai, H., Padture, N. P., Hooks, B. M. and Lawn, B. R., Flaw tolerance and toughness curves in two-phase particulate composites: SiC/glass system. *J. Eur. Ceram. Soc.*, 1994, **13**, 149–157.
29. Xu, H. H. K., Jahanmir, S., Ives, L. K., Job, L. S. and Ritchie, K. T., Short-crack toughness and abrasive machining of silicon nitride. *J. Am. Ceram. Soc.*, 1996, **79**(12), 3055–3064.
30. Kumar, A. and Eyre, B. L., Grain boundary segregation and intergranular fracture in molybdenum. *Proc. R. Soc. Lond.*, 1980, **A370**, 431–458.
31. Bartolome, J. F., Diaz, M., Moya, J. S., Saiz, E. and Tomsia, A. P., Mullite/Mo interfaces formed by intrusion bonding. *J. Eur. Ceram. Soc.*, 2004, **24**(5), 785–790.
32. Kameo K., New routes for tailoring metal- and ceramic-based composites for tribological applications, *PhD Thesis*, Institu für Verbundwerkstoffe, Technische Universität Kaiserslautern, Germany, 2005.
33. Pecharroman, C. and Moya, J. S., Experimental evidence of a giant capacitance in insulator conductor composites at the percolation threshold. *Adv. Mater.*, 2000, **12**(4), 294–297.
34. Outokumpu HSC Chemistry® for Windows, *Outokumpu Research*, Oy, Finland, 2002.
35. Gómez-Vega, J. M., Saiz, E., Tomsia, A. P., Oku, T., Suganuma, K., Marshall, G. W. *et al.*, Novel bioactive functionally graded coatings on Ti6al4V. *Adv. Mater.*, 2000, **12**(12), 894–898.
36. Tomsia, A. P., Moya, J. S. and Guitian, F., New route for hydroxiapatite coatings on Ti-based human implants. *Scripta Metallur. et Materialia*, 1994, **31**(8), 995–1000.
37. Hsieh, N. and Fine, M. E., The Lorenz and electron transport properties of NbO. *J. Appl. Phys.*, 1981, **52**(4), 2876–2883.
38. Feng, A. and Munir, A., Effect of product conductivity on field-activated combustion synthesis. *J. Am. Ceram. Soc.*, 1997, **80**(5), 1222–1230.